Measurement method for characterizing a millimeter-wave traveling-wave power combiner using *in-situ* test accessories

Honglei Sun [ID], Xiao-Wei Zhu [ID], Xuesong Shi [ID] and Ruijia Liu [ID]

School of Information Science and Engineering, Southeast University, Nanjing 210096, China

CAMBRIDGE
UNIVERSITY PRESS

Abstract

This paper presents a novel assessment method that minimizes test-fixture-induced errors in non-coaxial power combiner measurement by extending the port reduction method. This method involves terminating certain ports to acquire the scattering matrix of an N-port network from the scattering matrix measured at a reduced port order. The entire DUT scattering matrix is obtained from multiple scanning measurements, which are taken from partial coaxial accessible ports, based on a set of configurable terminating states. This advantage is leveraged to exclude a major portion of coaxial launch structures that would otherwise be incorporated in the conventional multiport test fixture. An analogous concept here is applied to measure a waveguide traveling-wave power combiner. A sandwiched twin structure, containing a divider/combiner pair with certain auxiliary through-type components cushioned between them, is utilized to assess the combiner characteristics. A theoretical framework of the proposed method was established to test its potential precision. Thereafter, an *in-situ* implementation was conducted to test its practical application on a traveling-wave combined amplifier prototype operating at the Q-band (33–39 GHz).

Introduction

In recent years, millimeter-wave (MMW) spectra (such as E-band, V-band, and Q-band) have been investigated for wireless backhauling application [1, 2]. These large continuous bandwidths provide a viable and cost-effective approach to data linkages between vast 5 G small cells and the core network. Waveguide power combiners are considered to boost the output power of MMW transmitters, to support their huge traffic load and atmospheric attenuation. The metal-pipe rectangular waveguide (MPRWG)-based power combiner [2–6] has lower loss than its planar transmission-line counterparts (such as the coplanar waveguide or microstrip). This merit makes MPRWG technology attractive for applications in which dissipative attenuation is critical. However, the manufacturing cost of such complex three-dimensional structures hinders their wider applications. This disadvantage is further exacerbated when the frequency moves upward to the MMW band. To overcome this constraint, several alternative manufacturing technologies for MMW MPRWG components [7–9] have been proposed, providing shorter lead-times, enhanced productivity, and reduced volume size. It is, however, essential that a cost-effective yet sufficiently accurate measurement technique is to be developed for low-cost, large-volume technology platforms to facilitate the widespread use of MMW MPRWG components.

The existing techniques for waveguide power combiner measurement fall into two main categories: hot tests (with driver unit amplifiers (UAs)) and cold tests. Hot tests require the coherent operation of numerous driver UAs, and thus are typically confined to final verification. Cold tests, conversely, provide economical alternatives for electrical performance monitoring and early fault detection. In term of hardware, a cold test is typically conducted by means of either a twin structure, comprising an interconnected, mirrored divider combiner, or a standalone combiner treated as a divider.

In the first cold test arrangement, although a back-to-back method is available for the two-port device under test (DUT) [10], there is currently no effective way to apply this method to multiport DUT cases. A slight variant of this method has been previously explored for the waveguide traveling-wave power combiner (TWPC) [11]; however, spikes on the frequency response proved to be problematic. Despite extra countermeasures to cope with the spikes, the application of this divide-by-two method to TWPC is confined to a limited frequency span.

In the second cold test arrangement, the non-coaxial interface of the combiner poses a critical obstacle to accurate scattering parameter measurement in terms of its densely populated parallel ports, the MMW operating frequency range and the resulting complexity of the test fixture. Due to the lack of a multiport counterpart for two-port thru-reflect-line calibration,
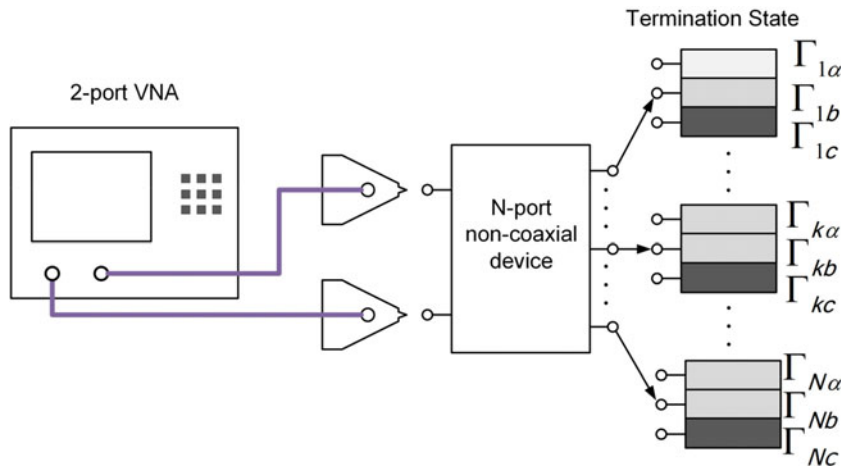
Fig. 1. Measurement setup for *N*-port non-coaxial device based on PRM method.

the necessary de-embedding to move the reference planes of a vector network analyzer (VNA) to the intrinsic ports is difficult. To minimize the burden of test fixture fabrication and modeling, an indirect multiport method, referred to as the "port reduction method" (PRM), is revised here, which can be utilized effectively for the scattering parameter measurement of *N*-port MPRWG devices with a two-port VNA.

As delineated in Fig. 1, only the partial ports of the DUT are extended to VNA inputs through the test fixture, significantly reducing the fixture complexity. Additionally, all remaining DUT ports (usually ports that are difficult to access, or cannot be reached directly) are terminated using configurable auxiliary terminators. Moreover, a thorough examination of the multiport DUT can be achieved by using prearranged reflections of auxiliary terminators. As a result, the entire DUT scattering matrix can be obtained from the measurements acquired from the partial ports. This is known as the PRM method, and its working principle has already been deduced in [12]. Therefore, considering the diverse configurable states of termination at an individual port, a set of well-chosen termination conditions should be established for measurement purposes. Multiple scanning measurements relying on these specified conditions provide sufficient intermediate data to reconstruct the entire scattering matrix of the DUT. Consequently, the obtained intermediate data (a set of low-dimensional matrix data) are utilized to reconstruct the DUT scattering matrix, which is an $(N + 1)$ dimensional matrix, using a reconstruction algorithm. For instance, experimental verification has been previously reported on an *X*-band eight-way busbar divider/combiner [13], as well as on an HDMI digital bus [14]. In brief, the validity of the PRM method relies on two foundational aspects [15]: an accurate model of a custom-made auxiliary termination and the robustness of the reconstruction algorithm. However, the accuracy of reconstruction algorithm tends to be unstable and, therefore, the ultimate accuracy of the PRM method is limited [16]. This issue of accuracy may be monitored and remedied by exploiting the respective condition number associated with the crucial matrix inversion operations inside the algorithm. In practice, large condition numbers commonly lead to ill-conditioned numerical calculations. This is the reason that remedial works of error detection and recalculation are often researched. Specifically, with respect to MMW MPRWG component, the PRM method normally relies on an augmented second tier of VNA calibration by means of dedicated calibration kits ([17, 18]) to minimize the post-calibration residual errors,

thereby ensuring accuracy. In summary, the two extant methods discussed above do not fully address the needs of TWPC characterization.

This paper proposes a cold test method, namely the "cushioned pair method", which accommodates the design refinement of a TWPC. The cushioned pair method is not limited in terms of bandwidth and its formulation includes an alternative reconstruction algorithm which does not necessitate the unsettled matrix inversion. An *in-situ* implementation was conducted to validate the effectiveness of the proposed method under real-world requirements.

This paper is organized as follows: section "Problem description and working principle of cushioned pair method" describes the general problem of characterizing a multiway TWPC and presents the principle of the proposed method. Although the theoretical framework of our method bears resemblance to that of a previous work [19], two crucial distinctions exist between the key formulas in this paper and that in the previous one. In brief, the improved expression has a wider applicable scope, making it better suited to the asymmetrical combiner exemplified by the TWPC. Moreover, a practical implementation of the cushioned pair method is quantitatively analyzed in section "Problem description and working principle of cushioned pair method". Section "Fabrication and measurement" reports a representative example of a *Q*-band MPRWG-based TWPC and delineates each step of the proposed approach. Section "Conclusions" provides a brief summary and conclusion.

Problem description and working principle of cushioned pair method

Introduction to the waveguide traveling-wave power combiner

The TWPC is an asymmetric longitudinal one-dimensional spatial power combiner, which is flexible in its number of amplifier channels. A physical model of a combined amplifier module utilizing a TWPC is presented in Fig. 2. Its essential components are highlighted in Fig. 2(a) and its schematic is presented in Fig. 2(b). Entering from the left side, the input signal is coupled from the waveguide divider onto each microstrip, thereafter reaching each UA. After amplification, the signals from each UA are combined at the TWPC on the right side via a reverse process. The assembly of its *E*-plane split-block is shown in Figs 2(c) and 2(d). The bulky metal walls of the waveguides are merged with chip carriers for
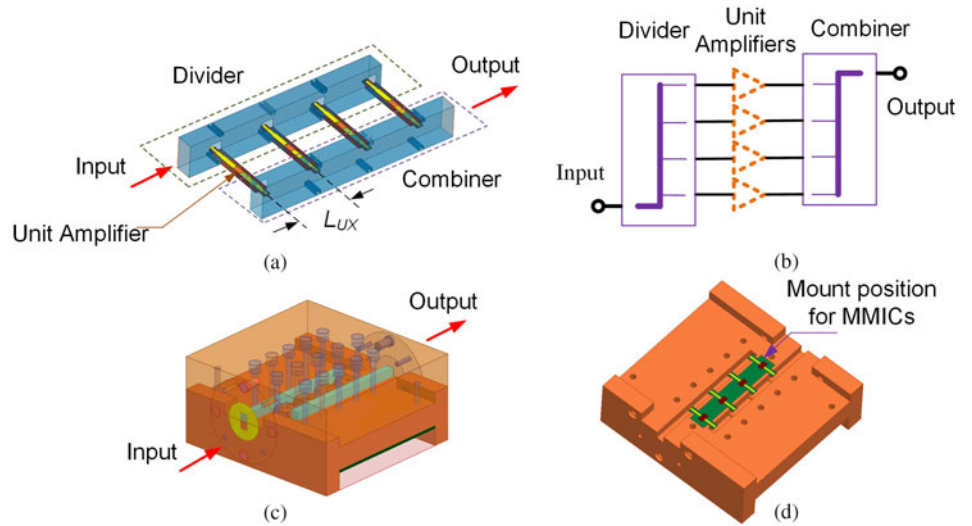
Fig. 2. Physical model of a combined amplifier module utilizing TWPC. (a) Essential components of a combined amplifier based on TWPC; (b) schematic diagram of the combined amplifier; (c) overall view of a representative combined amplifier module realized by E-plane split-block assembly; (d) bottom half of E-plane split-blocks.

MMICs to provide electrical and thermal conductivity. A PCB incorporating the planar *E*-plane probes is mounted above the metal base. A key indicator representing the compactness of the combiner is the interval distance L_{UX} (Fig. 2(a)). Its typical value is approximately $1/8 \lambda_G$, which is equal to 1.53 mm at a frequency of 36 GHz.

One of the advantages of the combiner, in addition to its low volume and weight, is that its compactness reduces the insertion loss. However, such compactness also gives rise to challenges in its testability. A compact combined amplifier module lacks sufficient space for a test fixture containing a parallel row of end-launch coaxial connectors in parallel [20]. An enlarged variant of the prototype in Fig. 2 can be built separately for measurement purposes, but *in-situ* measurement carried out on the prototype itself is more advantageous, due to its rapid operation and the elimination of the repeatability concern related to second sample fabrication. Rotational symmetry between the divider and combiner, illustrated in Fig. 2, was therefore utilized in this study to suit the proposed method.

Working principal of the cushioned pair method

In this study, an RF system in which multiple coherent sources collectively drive a single load through a passive $(N+1)$ port power-combining network, as shown in Fig. 3, was investigated. The input ports of the network are labeled sequentially while the output port is labeled "o". The network is represented by an $(N+1)$ dimensional S-matrix S^C, and a crucial vector (CV) $\vec{\zeta}$ within S^C is defined in equation (1) to facilitate subsequent deductions. The coherent sources are represented by an excitation signal vector (ESV) b^G, the components of which are denoted as b_k^G. Here, the power-combining efficiency of the power combiner termed as η_C is expressed in terms of $\vec{\zeta}$ and b^G in equation (2).
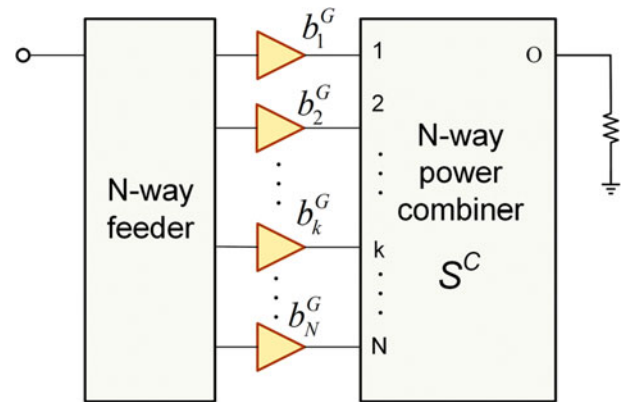
$$
S^C = \begin{bmatrix}
s_{11} & s_{12} & \cdots & s_{1N} & s_{1o} \\
s_{21} & s_{22} & \cdots & s_{2N} & s_{1o} \\
\vdots & \vdots & \ddots & \vdots & \vdots \\
s_{N1} & s_{N2} & \cdots & s_{NN} & s_{No} \\
\underbrace{s_{o1} \quad s_{o2} \quad \cdots \quad s_{oN}}_{\vec{\zeta}} & s_{oo}
\end{bmatrix}, \tag{1}
$$

Fig. 3. Representation of general *N*-way power-combining circuit.

$$
\eta_C = \left. \frac{\left| \sum s_{ok} \cdot b_k^G \right|^2}{\sum \left| b_k^G \right|^2} \right|_{k=1,2,\cdots,N} = \frac{1}{\left\| \vec{b^G} \right\|_2^2} \left\langle \vec{\zeta} \cdot \vec{b^G} \right\rangle. \tag{2}
$$

As per equation (2), combining efficiency η_C depends not only on the intrinsic property of the combiner (CV $\vec{\zeta}$), but also on the input signal (ESV b^G). According to the inner product computation in equation (2), the negative impact of numerical error propagation – as is manifested in the outcome of the accumulated error of η_C – increases along with the path amount N. Equation (2) can be rewritten to alleviate this by defining two sets of variables: magnitude variable κ_{k_s} and phase variable ρ_{k_s} as in equations (4a) and (4b), respectively.

$$
\eta_C = \left| \sum \left| b_k^G \right|^2 \kappa_k \cdot \exp \left(j \rho_j \right) \right|^2 \cdot \left\| \vec{\zeta} \right\|_2^2, \tag{3}
$$

$$
\kappa_k = \left(\frac{\left| s_{ok} \right|}{\left\| \vec{\zeta} \right\|_2} \right) \Bigg/ \left(\frac{\left| b_k^G \right|}{\left\| \vec{b^G} \right\|_2} \right), \tag{4a}
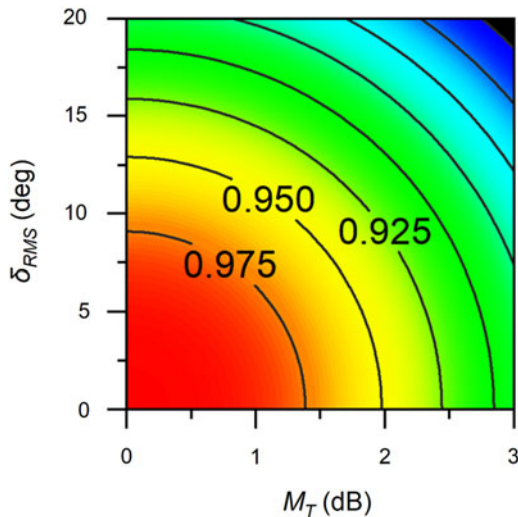$$

Fig. 4. Power-combining efficiency η_C contour plots associated with M_T and δ_{RMS}.

$$\rho_k = Arg(b_k^G \cdot s_{ok}). \tag{4b}$$

Next, the effect of $\kappa_k s$ and $\rho_k s$ within equation (3) can be represented by three statistical parameters of $\kappa_k s$ and $\rho_k s$, namely M_T, M_V, and δ_{RMS}, as defined over $\kappa_k s$ and $\rho_k s$ in equations (5a)–(5c); respectively. As a result, equation (3) is further reformulated as equations (6a)–(6d), thereby establishing a confidence interval estimation of η_C that supersedes the previous single point estimation. The individual contribution of each statistical parameter is also explicitly distinguishable. Specifically, the lower bound of η_C interval estimation, termed as H, is decomposed into three constituent factors: H^M, H^P, and H^D in equation (6a). These factors are provided individually. H^M, which represents the effect related to $\kappa_k s$, is mapped to a function of M_T and M_V. Similarly, H^P, which represents the effect related to $\rho_k s$, is mapped to a function of δ_{RMS}, while H^D represents the other effect of dissipative loss. By way of further clarification, *stddev* in equation (5c) represents the standard deviation function and *Geomean* in (6c) represents the geometric mean function. A proof of equations (6a)–(6d), based on general inequality theorems [21–24], is provided in the appendix.

$$M_T = \text{Max}(\kappa_1, \kappa_2, \cdots, \kappa_n), \tag{5a}$$

$$M_V = 1/\min(\kappa_1, \kappa_2, \cdots, \kappa_n), \tag{5b}$$

$$\delta_{RMS} = stddev(\rho_1, \rho_2, \cdots, \rho_n), \tag{5c}$$

$$\eta_c \geq H = H^M \cdot H^P \cdot H^D, \tag{6a}$$

$$H^M = \frac{4M_V M_T}{(1 + M_V M_T)^2}, \tag{6b}$$

$$H^P \approx [Geomean(\cos(\rho_1), \cdots, \cos(\rho_n))]^2, \\ \approx \cos^2(\delta_{RMS}) \tag{6c}$$

$$H^D = \left\| \vec{\zeta} \right\|_2^2. \tag{6d}$$

With respect to the practical application of the formulation in equations (6a)–(6d), H^D is usually determined once by the implementation process, in relation to the material properties or combiner architecture. H^D is therefore not considered during the design refinement process. H^M and H^P are closely related to the experimental design optimization of the combiner performance. In typical cases, H^P outweighs H^M as the dominant factor in η_C degradation.

To provide an intuitive understanding of equation (6), η_C dependence with respect to M_T and δ_{RMS} is illustrated in Fig. 4. The dependence of M_V is omitted due to the symmetrical form of equation (6b). Three contour lines (0.975–0.925) mark the most commonly used zone while the color maps represent the gradient vector. The 0.975 contour line, as an example, intersects the axes at M_T of 1.3 dB and δ_{RMS} of 9°.

The data collection process of $\kappa_k s$ and $\rho_k s$ is discussed in the next section.

In-situ *implementation and associated methodical errors*

The above methodology as it applies to a general power combiner was implemented in a TWPC (Fig. 2) by means of a set of test circuits. A flowchart of the three-step measurement procedure is shown in Fig. 5. The first measurement on circuit-A (Fig. 6(a)) was utilized to assess the overall performance of the power combiner. In the event of a defect within the combiner, although a declined overall performance can be observed, the position of the defect must also be located. As supplementary means, the latter two measurements on circuit-B and circuit-C (Figs 6(b) and 6(c), respectively) may be used successively to determine the position and severity of the defect.

Considering the resemblance between Figs 6 and 2(b), an *in-situ* realization of the test circuit (Fig. 6) was achieved by adopting miniature components. In this case, the space reserved for UAs (Fig. 2(d)) was reused. First, the reserved space could accommodate pairs of attenuator chips (Figs 6(a) and 6(b)). Second, the schematic in Fig. 6(c) can be realized in a similar way – although the original PCB (Fig. 2(d)) should be replaced by a subtly modified PCB to draw out the output voltages of the power detectors. The primary advantage of the *in-situ* implementation is that the planar transmission-line interface of the combiner is directly used, thereby avoiding a coaxial-to-non-coaxial fixture. This *in-situ* implementation also basically eliminates any methodical errors due to the inherently poor return loss of the TWPC input ports. A quantitative analysis of the methodical errors associated with this *in-situ* implementation is provided below for comparison against other methods.

First, a calculation equation of η_C was derived based on the cushioned pair structure in Fig. 6(a). Accordingly, the η_C outcome was determined by the composite transmission coefficient of the entire structure. The methodical error associated with the equation, termed as ε_η, is also provided here. Let α_L and α_R denote the attenuation value of the attenuator array on the left and right, respectively, and let S^D and S^C denote the scattering matrices of the power divider and combiner (Fig. 6(a)), respectively. To facilitate subsequent formulations, S^D and S^C are partitioned into block matrices in the form of equations (7a) and (7b), where S_{BB} and S_{CC} are matrices of order $n \times n$, and S_{AB} and S_{CD} are matrices of order $1 \times n$ and $n \times 1$, respectively. Diagonal matrices Λ_L and Λ_R are defined in equations (7c) and (7d) to represent the transmission response of the attenuators, wherein db2mag denotes the decibel to linear magnitude conversion function.
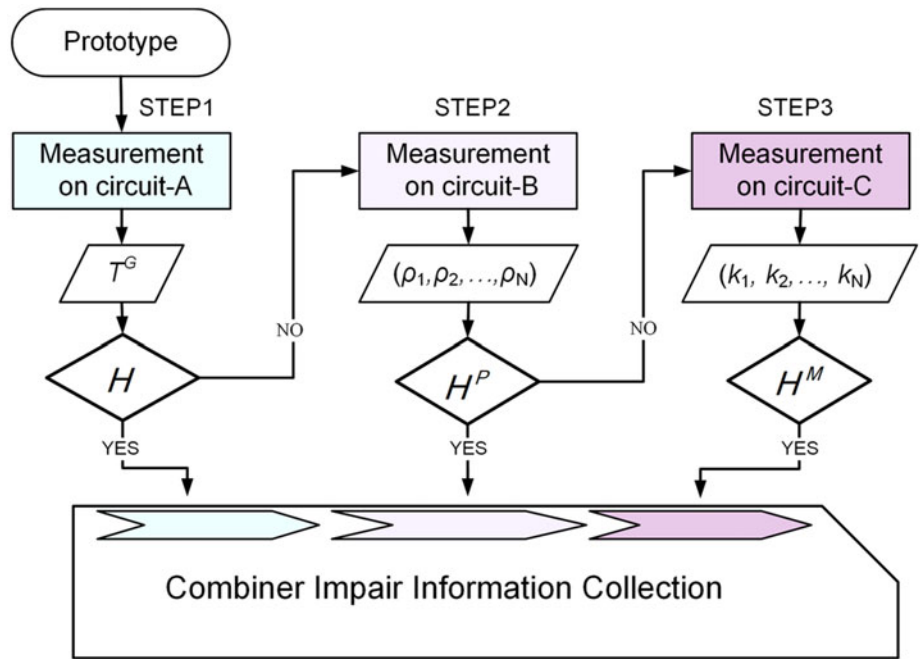
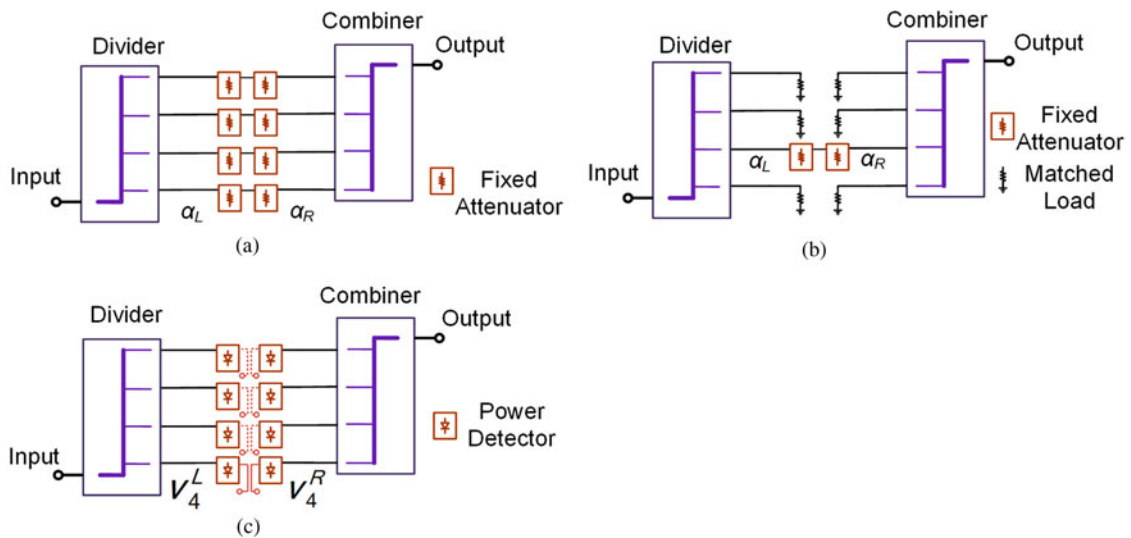**Fig. 5.** Flowchart of TWPC measurement during the design cycle.

Fig. 6. Schematic diagram of TWPC test circuits. (a) Schematic diagram of test circuit for η_C measurement marked as circuit A; (b) schematic diagram of test circuits for measurement of ρ_ks marked as circuit B; (c) schematic diagram of test circuits for measurement of κ_ks marked as circuit C.

Based on the above terms, the transmission coefficient of the entire structure in Fig. 6(a) (termed as T^G) is derived in equation (8) by means of the multiport network theory [25]. For ease of comparison, η_C is also expressed by S_{AB} and S_{CD} in equation (9). The comparison indicates that the middle term on the right side of equation (8), which is denoted as $f(\alpha_L, \alpha_R)$, impedes the calculation of η_C from T^G. In essence, the $f(\alpha_L, \alpha_R)$ function explicitly represents the damped multiple reflections within the structure.

$$S^D = \left[\begin{array}{c|c} S_{AA} & S_{AB} \\ \hline S_{BA} & S_{BB} \end{array} \right] \tag{7a}$$

$$S^C = \left[\begin{array}{c|c} S_{CC} & S_{CD} \\ \hline S_{DC} & S_{DD} \end{array} \right] \tag{7b}$$

$$\Lambda_L = \mathrm{db2mag}(-\alpha_L) \cdot U, \tag{7c}$$

$$\Lambda_R = \mathrm{db2mag}(-\alpha_R) \cdot U, \tag{7d}$$

$$T^G = S_{AB}\Lambda_L[U - (\Lambda_L S_{BB}\Lambda_L)(\Lambda_R \cdot S_{CC}\Lambda_R)]^{-1}\Lambda_R S_{CD}, \tag{8}$$
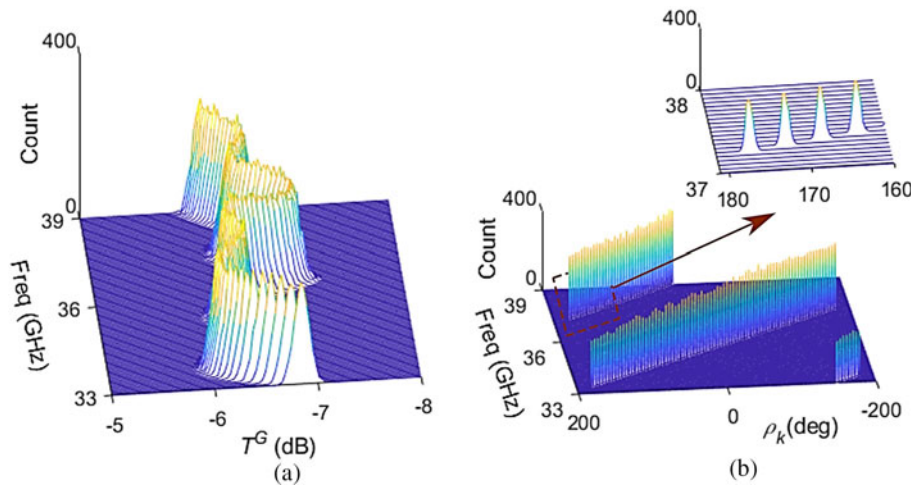
Fig. 7. Histograms of typical MC simulation results (1500 trials). (a) T^G fluctuation owing to attenuator variation; (b) ρ_k fluctuation owing to attenuator variation.

Table 1. Methodical errors of *in-situ* implementation under typical conditions

ε_η	ε_ρ	ε_κ
3.1%[a]	1.8°[a]	0.23–0.37 dB[b]

[a]Attenuation value $\alpha_L = \alpha_R = 6$ dB.
[b]Power detector [27] calibrated by power meter [28].

$$\eta_C = \frac{S_{AB}S_{CD}}{S_{AB}S_{AB}^T}. \tag{9}$$

To address this issue, $f(\alpha_L, \alpha_R)$ is first expanded into a Taylor series and, subsequently, matrix Taylor series truncation [26] is used to simplify the formula. The relation between η_C and T^G is thus established by linear approximation. The Taylor series expansion of $f(\alpha_L, \alpha_R)$ presented in equation (10a) is established only under its convergence condition, which is also provided alongside in equation (10b). The consequent calculation equation is shown in equation (11). The associated methodical error ε_η produced by the series truncation can also be estimated by means of the corresponding matrix spectral radius in equation (10b). For instance, when α_L and α_R are set to 6 dB, the produced ε_η is around 3.1%. In view of such a minor ε_η, the calculation of η_C from T^G may be considered to satisfy common requirements.

$$
\begin{aligned}
f(\alpha_L, \alpha_R) &= [U - (\Lambda_L S_{BB} \Lambda_L)(\Lambda_R S_{CC} \Lambda_R)]^{-1} \\
&= U + \sum_1^\infty (\Lambda_L S_{BB} \Lambda_L \cdot \Lambda_R S_{CC} \Lambda_R)^k \\
&\approx U,
\end{aligned}
\tag{10a}
$$

$$
\begin{aligned}
\|\Lambda_L S_{BB} \Lambda_L \cdot \Lambda_R S_{CC} \Lambda_R\|_2 &\leq \|\Lambda_L\|_2^2 \|\Lambda_R\|_2^2 \|S_{BB}\|_2 \|S_{CC}\|_2 \\
&\leq \text{db2mag}(-\alpha_L - \alpha_R),
\end{aligned}
\tag{10b}
$$

$$\eta_C = \text{db2mag}\left[\frac{(\alpha_L + \alpha_R)}{2}\right] \cdot \sqrt{|T^G|}. \tag{11}$$

Similarly, the methodical error related to $\rho_k s$, referred to as ε_ρ, can also be assessed by a Taylor series expansion. When α_L and α_R (Fig. 6(b)) are 6 dB, the resultant error ε_ρ is around 1.8°.
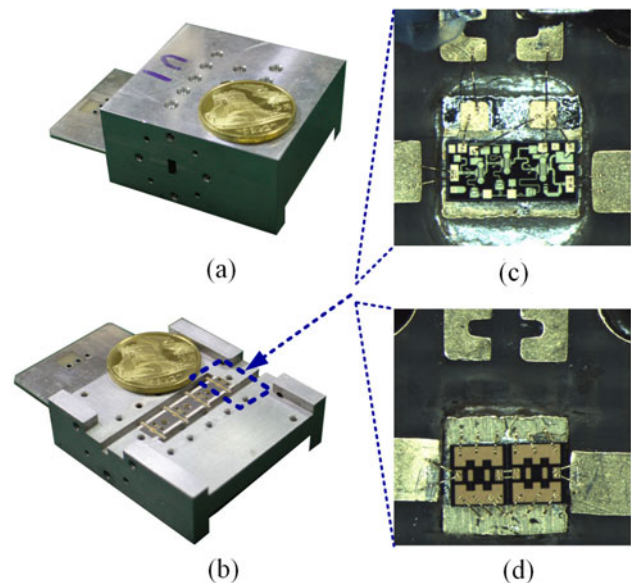

Fig. 8. Photograph of the fabricated prototype. (a) Photograph of entire combined amplifier module; (b) photograph of bottom half of E-plane split-blocks; (c) microphotograph of amplifier MMIC mounting; (d) microphotograph of chip attenuator mounting.

A quantitative analysis was also conducted in this study by means of Monte Carlo (MC) simulation with respect to the negative impact of attenuator variation. Considering the standard deviation values of $\delta(T^G)$ and $\delta(\rho_k)$ shown in Figs 7(a) and 7(b), respectively, the typical values are unveiled as $\delta(T^G) < 0.088$ dB and $\delta(\rho_k) < 0.19°$, on the condition that regular chip attenuators are employed. These modest values suggest that the impact of attenuator variation is estimable and treatable.

The methodical error of $\kappa_k s$ (termed as ε_κ) is determined from the expression of $\kappa_k s$ in equation (12), wherein γ_V is the voltage sensitivity of the power detectors, while v_k^L and v_k^R are output voltages of the power detectors in Fig. 6(c).

$$\kappa_k = \left(\frac{1}{\gamma_V}\right) \cdot \left(\frac{v_k^R}{v_k^L}\right) \tag{12}$$
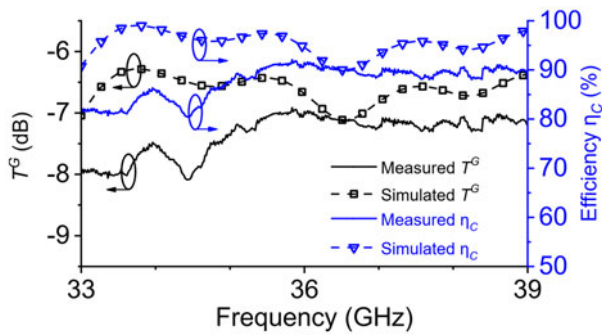
Fig. 9. Simulated and measured transmission coefficient T^G and corresponding η_C values.

The main error source of ε_κ is ascribed to γ_V, whereas the contributions of v_k^L and v_k^R are negligible. To enhance the accuracy of γ_V, the response of a power detector is usually calibrated by a power meter. Therefore, the error of γ_V depends on individual variations in a set of power detector, as well as the error of the power meter. In a typical case at the MMW band, the variation [27] contributes 0.10–0.20 dB, while the power meter error [28] contributes 0.13–0.17 dB to ε_κ. Thus, a typical ε_κ ranges from 0.23 to 0.37 dB.

The typical values of the three error terms discussed above are listed in Table 1. The proposed method provides sufficient precision for regular applications. The specific requirements of auxiliary hardware can also be determined according to the targeted measurement deviations.

Fabrication and measurement

A Q-band four-way waveguide TWPC with a 33–39 GHz operational frequency was evaluated by means of the proposed method. Photographs of the entire prototype module, as well as microphotographs of the chip mounting, are provided in Fig. 8. Split-block geometries of the waveguide combiner and UAs are shown in Figs 8(a) and 8(b). Microphotographs of the amplifier MMIC mounting and chip attenuator mounting are shown in Figs 8(c) and 8(d), respectively.

The mechanical part of the waveguide TWPC was fabricated on a 6061 aluminum alloy plate by a computer numerical control machining. A conventional carbide drill was used for the cut. The positional accuracy of the device is 20 μ and the roughness R_a (arithmetic mean surface roughness) is within a range of between 0.8 and 1.6 μ. The E-probe array and microstrip were realized on 0.254 mm-thick TLY-5 substrate (Taconic) with 17 μm electrode-posited copper cladding.

The *in-situ* implementation of the test circuits (Figs 6(a) and 6(b)) is shown as a close-up photograph in Fig. 8(d) in the context of Fig. 8
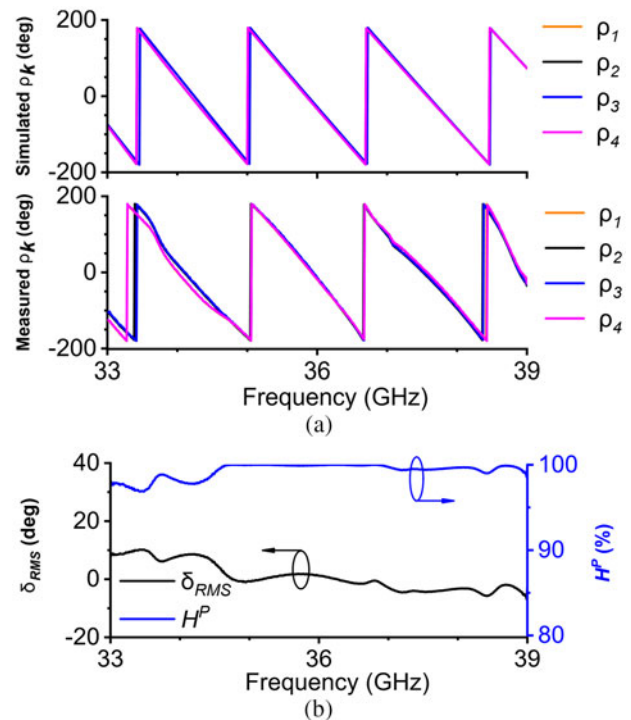

Fig. 10. Simulated and measured data of ρ_ks along with measured δ_{RMS} and H^P. (a). Frequency response of simulated and measured ρ_ks. (b). Frequency response of measured δ_{RMS} and H^P.

(b). A thin film attenuator ATN3580 series (Skyworks) [29] was used in the test circuits. To facilitate the measurements, 6 dB attenuators were used consistently for the through path, while 12 dB attenuators of equal footprint were used for load termination (Fig. 6(b)). Switching from the test circuits shown in Fig. 6(a) to those shown in Fig. 6(b) was achieved simply by replacing the passive chips. The dimensions of the PCB apertures for MMIC are 2.15×1.80 mm, and the footprint of the attenuator is 0.69×0.74 mm. The measurements were accomplished by means of a two-port VNA with a pair of WR-22 waveguide-to-coax adapters.

Figure 9 shows both the simulated and measured data of the transmission coefficient T^G and their derived values of power-combing efficiency η_C. The simulated data were obtained by co-simulation with Ansys HFSS and Keysight ADS. The gap between the simulated and measured results reflects mainly the extra conductive loss owing to the random rough metal surface. The measured power-combining efficiency η_C is close to 90%, with the exception of a slight dip at the low end of the frequency span. Based on an empirical estimation, the measured η_C of the prototype is consistent with the expected value derived from the process capabilities of the constituent parts: the MPRWG component by an E-plane split-block process [30, 31] and a planar E-plane probe [32]. Furthermore, the η_C performance of this

Table 2. Comparison with previous methods

Ref	Coaxial launcher amount	Fabrication lead-time	Computation complexity	Applicability to miniaturized combiner
[33]	$N + 1$	Long	Low	✗
[13]	$2 \leq q < N$	Medium	High	√
This work	2	Short	Low	√

prototype is relatively close to that of a counterpart with a more sophisticated process [33].

Figure 10(a) shows the simulated and measured phase shift $\rho_k s$ of the individual branches. Figure 10(b) provides the δ_{RMS} and H^P values obtained from measured $\rho_k s$. In view of the consistent curves in Figs 8 and 10(b), the frequency responses of η_C and H^P are in sufficiently close agreement. Taken together, these data may provide a workable reference for the further TWPC design refinement. For instance, according to the value of $\rho_k s$, suitable phase trimmers [11] can be attached to the input interface of the TWPC.

The $\kappa_k s$ measurement depicted in Fig. 6(c) remains unfinished due to a shortage of power detector chips. Although the data of $\kappa_k s$ and their corresponding H^M values are absent, the proposed method is still delineated by this example because the contribution of H^M is independent and subordinate to H^P, as indicated by the contour plot in Fig. 4. In addition, the contribution of H^M in this example is minor owing to the attractive coupling mechanism of the E-plane waveguide probe (which has been evaluated empirically in [34]). Assuming that the waveguide TWPC is realized in an alternative form of longitudinal slots [35, 36], a less agreeable κ_k characteristic should emerge due to its more complex coupling mechanism, thus enlarging H^M.

Table 2 shows a comparison of the cushioned pair method against other state-of-the-art methods at the MMW band. The most notable advantages of the proposed method include quicker hardware fabrication and simpler post processing of the acquired data.

Conclusions

This paper presents the cushioned pair method for MMW TWPC characterization up to the intrinsic ports. The primary advantage of this method is that all measurements are performed *in-situ*, thereby precisely revealing all impacting factors in real time. The prototype fabrication and measurement processes under the proposed method can also be accelerated by supplementary commercial off-the-shelf components, thereby precluding the time-consuming work of fabricating and modeling customized terminators.

References

1. **Dehos C, González JL, De Domenico A, Ktenas D and Dussopt L** (2014) Millimeter-wave access and backhauling: the solution to the exponential data traffic increase in 5 G mobile communications systems? *IEEE Communications Magazine* **52**, 88–95.
2. **Pi Z, Choi J and Heath R** (2016) Millimeter-wave gigabit broadband evolution toward 5G: fixed access and backhaul. *IEEE Communications Magazine* **54**, 138–144.
3. **Yu CF and Chang TH** (2005) High-performance circular TE_{01}-mode converter. *IEEE Transactions on Microwave Theory and Techniques* **53**, 3794–3798.
4. **Chang TH, Li CH, Wu CN and Yu CF** (2010) Generating pure circular TE_{mn} modes using Y-type power dividers. *IEEE Transactions on Microwave Theory and Techniques* **58**, 1543–1550.
5. **Guo L, Li J, Huang W, Shao H and Ba T** (2017) A compact four-way power combiner. *IEEE Microwave and Wireless Components Letters* **27**, 239–241.
6. **Guo L, Li J, Huang W, Shao H, Ba T, Xie S, Jiang Y and Deng G** (2018) Design of compact high-isolation four-way power combiners. *IEEE Transactions on Microwave Theory and Techniques* **66**, 2185–2198.
7. **Zhang B and Zirath H** (2016) A metallic 3-D printed E-band radio front end. *IEEE Microwave and Wireless Components Letters* **26**, 331–333.
8. **Chan KY, Ramer R and Sorrentino R** (2018) Low-cost ku-band waveguide devices using 3-D printing and liquid metal filling. *IEEE Transactions on Microwave Theory and Techniques* **66**, 1–9.
9. **Ermolov V, Lamminen A, Saarilahti J, Wälchli B, Kantanen M and Pursula P** (2018) Micromachining integration platform for sub-terahertz and terahertz systems. *International Journal of Microwave and Wireless Technologies* **10**, 651–659.
10. **Martens J** (2009) Common adapter/fixture extraction techniques: sensitivities to calibration anomalies. *74th ARFTG Microwave Measurements Conference*, Broomfield, CO.
11. **Li LA, Hilliard BJ, Shafer JR, Daggett J, Dickman EJ and Becker JP** (2008) A planar compatible traveling-wave waveguide-based power divider/combiner. *IEEE Transactions on Microwave Theory and Techniques* **56**, 1889–1898.
12. **Rolfes I and Schiek B** (2005) Multiport method for the measurement of the scattering parameters of N-ports. *IEEE Transactions on Microwave Theory and Techniques* **53**, 1990–1996.
13. **Lonac JA, Melczarsky I and Paganelli RP** (2011) Simple method for characterizing linear multi-port microstrip structures. *International Journal of Microwave and Wireless Technologies* **3**, 281–288.
14. **Kam DG and Kim J** (2007) Multiport measurement method using a two-port network analyzer with remaining ports unterminated. *IEEE Microwave and Wireless Components Letters* **17**, 694–696.
15. **Chen CJ and Chu TH** (2009) Measurement of noncoaxial multiport devices up to the intrinsic ports. *IEEE Transactions on Microwave Theory and Techniques* **57**, 1230–1236.
16. **Chen CJ and Chu TH** (2011) Accuracy criterion for S-matrix reconstruction transforms on multiport networks. *IEEE Transactions on Microwave Theory and Techniques* **59**, 2331–2339.
17. **Jargon JA, Arz U and Williams DF** (2012) Characterizing WR-8 waveguide-to-CPW probes using two methods implemented within the NIST Uncertainty Framework. *80th ARFTG Microwave Measurements Conference*, San Diego, CA.
18. **Judaschke RH** (2011) Second-order waveguide calibration of a one-port vector network analyzer. *77th ARFTG Microwave Measurements Conference*, Baltimore, MD.
19. **Gupta MS** (1992) Degradation of power combining efficiency due to variability among signal sources. *IEEE Transactions on Microwave Theory and Techniques* **40**, 1031–1034.
20. "PE45402 datasheet," Pasternack, Irvine, CA, USA, rev. 1.4, 2018. [Online]. Available at https://www.pasternack.com/1.85mm-female-end-launch-pcb-connector-pe45402-p.aspx.
21. **Drachman BC and Cloud MJ** (2014) *Inequalities: With Applications to Engineering*, 2nd Edn. New York: Springer.
22. **Moskowitz MA and Paliogiannis F** (2011) *Functions of Several Real Variables*. Singapore: World Scientific.
23. **Diaz JB and Metcalf FT** (1964) Complementary inequalities. I: Inequalities complementary to Cauchy's inequality for sums of real numbers. *Journal of Mathematical Analysis and Applications* **9**, 59–74.
24. **Mitrinovic DS, Pecaric J and Fink AM** (1993) *Classical and New Inequalities in Analysis*, vol. **61**. Dordrecht, The Netherlands: Kluwer Academic Publishers.
25. **Mongia R, Bahl I and Bhartia P** (1999) *RF and Microwave Coupled-Line Circuits*. Norwood, MA: Artech House.
26. **Higha NJ** (2008) *Functions of Matrices: Theory and Computation*. Philadelphia: SIAM.
27. "MADT-011000-DIE datasheet," Macom, Lowell, MA, USA, rev.V1, 2018 [Online]. Available at http://www.macom.com/products/product-detail/MADT-011000-DIE.
28. "R&S NRP-Z power sensor family specifications," Rohde & Schwarz, Munich, Germany, Version 10.00, May 2014 [Online]. Available at https://www.rohde-schwarz.com/us/brochure-datasheet/nrpz/.
29. "ATN3580 Series Fixed Attenuator datasheet," Woburn, MA, USA, 2018 [Online]. Available at http://www.skyworksinc.com/Products_Attenuators_FAP.aspx.

30. **Stil I, Fontana AL, Lefranc B, Navarrini A, Serres P and Schuster KF** (2012) Loss of WR10 waveguide across 70–116 GHz. In *Proc. 22nd Int. Symp. Space Terahertz Technol.*, Tokyo, Japan, pp. 2–4.

31. **D'Auria M, Otter WJ, Hazell J, Gillatt BT, Long-Collins C, Ridler NM and Lucyszyn S** (2015) 3-D printed metal-pipe rectangular waveguides. *IEEE Transactions on Components, Packaging, and Manufacturing Technology* **5**, 1339–1349.

32. **Samoska LA** (2011) An overview of solid-state integrated circuit amplifiers in the submillimeter-wave and THz regime. *IEEE Transactions on Terahertz Science and Technology* **1**, 9–24.

33. **Chu QX, Kang ZY, Wu QS and Mo DY** (2013) An in-phase output Ka-band traveling-wave power divider/combiner using double ridge-waveguide couplers. *IEEE Transactions on Microwave Theory and Techniques* **61**, 3247–3253.

34. **Eshrah IA, Kishk AA, Yakovlev AB and Glisson AW** (2006) Equivalent circuit model for a waveguide probe with application to DRA excitation. *IEEE Transactions on Antennas and Propagation* **54**, 1433–1441.

35. **Jiang X, Ortiz SC and Mortazawi A** (2004) A Ka-band power amplifier based on the traveling-wave power-dividing/combining slotted-waveguide circuit. *IEEE Transactions on Microwave Theory and Techniques* **52**, 633–639.

36. **Pérez JAG, Kosmopoulos S and Goussetis G** (2017) A compact 12-way slotted waveguide power combiner for Ka-band applications. *IEEE Microwave and Wireless Components Letters* **27**, 135–137.

Honglei Sun received his B.S. degree in Electronic Engineering in 2004 from Tianjin University, Tianjin, China. He is currently working toward his Ph.D. at the State Key Laboratory of Millimeter Waves, Southeast University, Nanjing, China. His research interests include RF/microwave/millimeter-wave power amplifiers (PA) and linearized transmitters for wireless communication. From 2005 to 2008, he held a Development Engineer position with Huawei Technology, where he was involved in the design of PAs for the GSM macro base-station. From 2011 to 2013, he was employed as a radio design engineer with Ericsson China, where he was involved in several power amplifier projects for WCDMA and LTE base-station.

Xiao-Wei Zhu (S'88-M'95) received his M.E. and Ph.D. degrees in Radio engineering from Southeast University, Nanjing, China in 1996 and 2000, respectively. He has been with Southeast University since 1984, where he is currently a professor at the School of Information Science and Engineering. Dr. Zhu has authored and co-authored more than 90 technical publications, and holds 15 patents. His research interests include RF and antenna technologies for wireless communications, microwave and millimeter-wave theories and technologies, as well as power amplifier (PA) non-linear character and its linearization research with a particular emphasis on wideband and high-efficiency GaN PAs. Dr. Zhu is the President of the Microwave Integrated Circuits and Mobile Communication Sub-Society, the Microwave Society of CIE, and Secretary of the IEEE MTT-S/AP-S/EMC-S Joint Nanjing Chapter.

Xuesong Shi was born in Xi'an, Shaanxi Province, China, in 1993. He received the B.S. degree in Communication Engineering from Southeast University in 2016 and he is currently working toward his M.S. degree at the State Key Laboratory of Millimeter Waves, Southeast University, Nanjing, China. His specific focus is electromagnetic field and microwave technology, and his study direction includes RF/microwave passive circuits such as filters, couplers, and mixers.
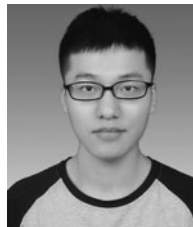
Ruijia Liu was born in Nanjing, Jiangsu Province, China, in 1995. He received his B.S. degree in Electronic Information Science and Technology from Southwest Jiaotong University, Chengdu, China, in 2017. He is currently working toward his Ph.D. degree at the State Key Laboratory of Millimeter Waves, Southeast University, Nanjing, China. His research interests include wideband microwave PA design and wideband millimeter-wave PA MMIC design.

Appendix

The lower bound of η_C is established through its decomposition into a product of two factors: η_a related to ρ_ks and η_b related to κ_ks. With respect to η_a, the superimposed effects of ρ_ks rely solely on $(\rho_k - \bar{\rho})$, the relative deviation from their mean value, which is termed as δ_k in equation (A2). Thereupon, the η_C expression in equation (A1) is decomposed into separated expressions of η_a and η_b, given in equations (A3) and (A4).

$$\eta_C = \eta_a \cdot \eta_b = \left| \sum \left| b_k^G \right|^2 \kappa_k \cdot \exp\left(j\rho_j\right) \right|^2 \cdot \left\| \vec{\zeta} \right\|_2^2, \tag{A1}$$

$$\delta_k = \rho_k - \bar{\rho}, \tag{A2}$$

$$\eta_a = \frac{\left| \sum \left| b_k^G s_{ok} \right| \exp\left(j\rho_k\right) \right|^2}{\left(\sum \left| b_k^G s_{ok} \right| \right)^2}$$
$$= \frac{\left| \sum \left| b_k^G s_{ok} \right| \exp\left(j\delta_k\right) \right|^2}{\left(\sum \left| b_k^G s_{ok} \right| \right)^2}, \tag{A3}$$

$$\eta_b = \frac{\left(\sum \left| b_k^G s_{ok} \right| \right)^2}{\sum \left| b_k^G \right|}. \tag{A4}$$

η_a can be bound as follows: since the magnitude of a complex number is no less than its real part, η_a in equation (A3) is estimated by equation (A5). Subsequently, the weighted arithmetic mean-geometric mean (weighted AM-GM) inequality theorem [21] is applied to equation (A5), thereupon inducing equation (A6). The superscripts in equation (A6), namely the weight factors, are already normalized and their sum is 1.

$$\eta_a \geq \frac{\left| \sum \left| b_k^G s_{ok} \right| \cos\left(\delta_k\right) \right|^2}{\left(\sum \left| b_k^G s_{ok} \right| \right)^2}, \tag{A5}$$

$$\eta_a \geq \left[\prod \cos\left(\delta_k\right)^{\left| b_k^G s_{ok} \right| / \left\| b_k^G s_{ok} \right\|_1} \right]^2. \tag{A6}$$

In practical cases, the values of these weight factors are close to each other because power combiners are usually designated for identical driving amplifiers. For this reason, these weight factors may be approximated as $1/N$, leading to the geometric mean function in equation (A7). In this case, the contributions of κ_ks to η_a are completely omitted.

$$\eta_a \geq \left[\prod \cos\left(\delta_k\right)^{1/N} \right]^2$$
$$= [Geomean(\cos\left(\delta_1\right), \cos\left(\delta_2\right), \cdots)]^2.$$

Intuitively, a root mean square (RMS) function is somewhat similar to a geometrical mean function; the RMS mean is usually preferable. An RMS alternative of equation (A7), which is expressed in equation (A8), is developed

to enable a quicker calculation.

$$\eta_a \geq [Geomean(\cos(\delta_1), \cos(\delta_2), \cdots)]^2$$
$$\approx [\cos(\sigma_{RMS})]^2. \tag{A8}$$

Additionally, the approximate equality between (A7) and (A8) can be proved by the Taylor's theorem in multiple variables [22]. Let $\delta = (\sigma_1, \cdots, \sigma_N)$ and consider two functions, $g(\vec{\delta})$ and $(\vec{\delta})$, as expressed in equations (A9) and (A10). In the ball zone around $\vec{z_r} = (0, \cdots, 0)$, a comparison between $g(\vec{\delta})$ and $f(\vec{\delta})$ can be carried out based on the first-order multivariable Taylor series expansion. The approximate equality can then be identified through the cross-examination of $g(\vec{z_r})$ and $f(\vec{z_r})$ in equation (A12) and that of the derivatives in equations (A13) and (A14).

$$g(\vec{\delta}) = \prod \cos(\delta_k)^{1/N}, \tag{A9a}$$

$$f(\vec{\delta}) = \cos\left[\left(\frac{1}{N} \cdot \sum \delta_k^2\right)^{1/2}\right], \tag{A9b}$$

$$f(\vec{\delta}) = f(\vec{z_r}) + \nabla f(\vec{\delta}) \cdot (\vec{\delta} - \vec{z_r}), \tag{A10a}$$

$$f(\vec{z_r}) = g(\vec{z_r}) = 1, \tag{A10b}$$

$$\frac{\partial g}{\partial \delta_k} = \left(-\frac{1}{N}\right) \cdot g(\vec{\delta}) \cdot \tan(\delta_k), \tag{A11a}$$

$$\frac{\partial f}{\partial \delta_k} = \left(-\frac{1}{N}\right)\left[\frac{\sin(\delta_{RMS})}{\delta_{RMS}}\right] \cdot \delta_k. \tag{A11b}$$

Next, a lower bound for η_b can be generated as follows: initially, the κ_k range defined in equations (5a) and (5b) is restated into a single in equation (A12). Subsequently, equation (A12) is utilized to deduce equation (A13), which meets a weak precondition for the certain inequalities theorem complementary to Cauchy's inequality [23, 24].

$$\frac{1}{M_V} \leq \kappa_k \leq M_T, \tag{A12}$$

$$|b_k^G|^2\left(\kappa_k - \frac{1}{M_V}\right)(M_T - \kappa_k)\left(\|\zeta\|_2^2 / \|b^G\|_2^2\right)$$
$$= \left(|s_{ok}| - \frac{1}{M_V}|b_k^G|\right)\left(M_T|b_k^G| - |s_{ok}|\right) \tag{A13}$$
$$\geq 0.$$

Equation (A14) is then derived from equation (A13).

$$\frac{\left(\sum |b_k^G s_{ok}|\right)^2}{\sum |b_k^G|^2 \cdot \sum |s_{ok}|^2} \geq \frac{4 M_T M_V}{(1 + M_T M_V)^2}. \tag{A14}$$

By combining equations (A14) and (A3), a lower bound for η_b can be derived in equation (A15).

$$\eta_b \geq \frac{4 M_T M_V}{(1 + M_T M_V)^2} |\zeta|_2^2. \tag{A15}$$

In summary, substitution of equations (A8) and (A15) into equation (A1) yields the lower bound of the combining efficiency η_C in equations (6a)–(6d).